Sheffield Hallam University

The Theory of Critical Distances to assess the effect of cracks/manufacturing defects on the static strength of 3D-printed concrete.
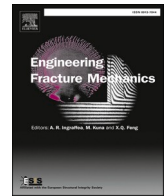
ALANAZI, N, KOLAWOLE, JT, BUSWELL, R and SUSMEL, Luca

Citation:

The Theory of Critical Distances to assess the effect of cracks/manufacturing defects on the static strength of 3D-printed concrete

N. Alanazi [a,b], J.T. Kolawole [c], R. Buswell [c], L. Susmel [a,*]

[a] *Department of Civil and Structural Engineering, The University of Sheffield, Mappin Street, Sheffield S1 3JD, United Kingdom*
[b] *Department of Civil Engineering, College of Engineering, University of Hail, Hail 81411, Saudi Arabia*
[c] *School of Architecture, Building and Civil Engineering, Loughborough University, Loughborough LE11 3TU, United Kingdom*

ABSTRACT

The present paper deals with the use of the Theory of Critical Distances to model the detrimental effect of cracks and manufacturing defects in 3D-printed concrete subjected to static loading. The robustness of the proposed approach was assessed against a number of experimental results that were generated by testing, under three-point bending, 3D-printed rectangular section specimens weakened by saw-cut crack-like sharp notches, surface roughness (due to the extrusion filaments) and manufacturing defects. The sound agreement between experiments and predictive model allowed us to demonstrate that the Theory of Critical Distances is not only a reliable design approach, but also a powerful tool suitable for guiding and informing effectively the additive manufacturing process.

1. Introduction

Large-scale additive manufacturing using concrete has experienced an exponential growth in uptake through patent applications, full-scale demonstration projects and academic publications [1–3]. The Technology Readiness Level has been estimated to be in between 6 and 7, similar to those found in main stream additive manufacturing [2,3].

These processes are typically deployed for the procurement of architecture, infrastructure and construction. There are a number of additive manufacturing approaches that map well onto those found in conventional additive manufacture, the recent assessment of the process-based classification of these methods map them on existing iso-standards [4]. Processes that make use of premixed concrete, or more typically, cement-based mortars through spraying, or jetting methods and through extrusion are the most common. Extrusion, similar to fused deposition modelling in principle is the most widely deployed.

The technology is used to produce products or parts of building structures across a whole range of scales. These can include printing street furniture, through to printing the walls of buildings. Additionally many infrastructure applications are also being explored such as drainage inspection covers, even bases for wind-turbines. Parts can typically be many hundreds of kilos in mass, and be measured in multiples of metres. Fig. 1 illustrates just some of the large scale applications that have been demonstrated.

The technology is maturing quickly [5–7] and academic and commercial communities are moving towards standardisation: for quality control of the material; understanding the geometric tolerances that can be achieved in manufacture; and evaluating the

---

* Corresponding author.
  E-mail address: l.susmel@sheffield.ac.uk (L. Susmel).

Nomenclature

A	crack length
B	specimen's thickness
F	force
F_f	failure force
K_C	fracture toughness
K_{IC}	plane strain fracture toughness
K_I	Mode I stress intensity factor
$K_{I,FEM}$	Mode I stress intensity factor determined numerically
K_{IC}	plane strain fracture toughness
L	critical distance
O_s	offset distance locating the fracture section
Oxy	local system of coordinates
S	span
W	specimen's width
α	shape factor
θ_p	angle between 3D-printing filaments and specimen's longitudinal axis
σ_y	normal stress parallel to axis y
$\sigma_{y,FEM}$	normal stress parallel to axis y determined numerically
σ_{eff}	effective stress
σ_f	nominal gross stress in the incipient failure condition
σ_{FS}	plain material flexural strength
σ_{nom}	nominal gross stress
σ_{UTS}	ultimate tensile strength

mechanical properties of the printed material.

In a similar way to the impact of additive manufacturing on standard materials [1–4], printed concrete introduces an anisotropy in the hardened material properties [8–11]. In addition, the variation of print quality and the inclusion of void within the material complicates matters [5,6,12] as it does in conventional additive manufacturing [13].

The anisotropy of extrusion-based 3D-printed concrete is one of the bottle necks for designers and early adopters of the technology. The mechanical properties of additively manufactured concrete differ from that of conventionally cast concrete, depending on the direction of loading relative to print direction. Loads perpendicular to the printing direction reduce the mechanical response and properties of 3D-printed concrete. Currently, a 1:1 scale of the intended structure usually requires testing in-order to obtain the mechanical properties that are required for design and government approval. At the root of this anisotropic property is the bond between extruded filaments of concrete, referred to as interlayer bond strength [7,14]. The bond can be weakened, causing the structure to behave non-monolithically under stress.

This is similar to the well-known cold jointing in traditional cast concrete, where old concrete tends not to be well bonded to a new concrete when the initial setting time of the old concrete is exceeded. In the case of additively manufactured concrete, the weak bond between successive layers is a combination of both materials and process related factors. The requirements for printable concrete materials result in the use of stiff (and accelerated) mixtures [8,9] that limits the availability of internal surface moisture essential to concrete bonding [7]. Evaporation of the surface moisture due to environmental conditions worsens this effect [10]. Process related factors centre around volume flow rate and robot dynamics. The print speed must match the pump flow output to avoid filament thinning, whilst the sudden change in the robotic arm toolpath direction must be minimised to reduce ramp up/down (and consequently the rate of deposited volume).

The major consequence of these factors is the preclusion of voids at the interfaces of successively extruded filaments in 3D-printed concrete, weakening the bond. Voids have been reported to be concentrated in the interlayer regions of printed parts and linked to the anisotropy of mechanical properties [5,10]. The generated voids reduce the mechanical properties of additively manufactured concrete in the transverse direction of the filaments' interface as shown in Fig. 2.

Understanding and predicting the deviation of these properties from that of conventional cast concrete is critical if design tools are to be deployed to model failure of this material and so realise the full potential of the technology. The majority of research has focused on determining the compressive, tensile and flexural strength of 3D-printed concrete with no direct links to that of the cast concrete. Widespread adoption of the technology will occur if designers and engineers can evaluate the anisotropy of additively manufactured concrete from that of the cast concrete. This is also crucial to developing design codes for structural 3D-printed concrete.

In the challenging scenario briefly depicted above, the present paper summarises an attempt to develop a novel design tool based on the Theory of Critical Distances [15] suitable for assessing the detrimental effect of cracks and manufacturing defects in additively manufactured concrete.

2. The Theory of Critical Distances to model defects/cracks in engineering materials

The Theory of Critical Distances (TCD) [15] is an overarching design philosophy postulating that static [16–18], dynamic [19] and fatigue [20,21] strength of flawed, cracked and notched engineering materials can be assessed accurately via specific length scale parameters [22]. In this setting, the critical length used in the design process is thought of as a physical property that is linked with the micro-/meso-/macro-structural characteristics of the material being assessed as well as with the specific features of the processes resulting in final breakage [15,23].

One of the distinctive traits of the TCD is that strength is assessed by reanalysing the linear-elastic stress fields damaging the material regions in close proximity to the assumed critical locations [15]. This *modus operandi* applies also to those materials whose failures are preceded by non-linear deformations (such as, for instance, plasticity in ductile metals) [18,24,25].

In a number of recent studies [26–29] it has been proven that the TCD is successful in estimating also the strength of notched cast concrete subjected to either static, dynamic or fatigue loading. In particular, based on comprehensive experimental investigations, it was proven that a high level of accuracy can be achieved by modelling un-reinforced concrete simply as a homogenous, isotropic, liner-elastic material.

As far as static assessment is concerned, the TCD quantifies damage through an effective stress, σ_{eff}, which is calculated by post-processing the entire linear-elastic stress field acting on a specific material region [15]. In this framework, the critical distance used to calculate the TCD effective stress can directly be estimated via the following widely-used relationship [15,16]:

$$L = \frac{1}{\pi}\left(\frac{K_{IC}}{\sigma_{UTS}}\right)^2 \tag{1}$$

In Eq. (1) K_{IC} is the plane strain fracture toughness, whereas σ_{UTS} is the material ultimate tensile strength. Since both K_{IC} and σ_{UTS} are mechanical properties, definition (1) makes it evident that critical length L is in turn a material physical constant [15].

From a physical modelling viewpoint, the TCD critical distance can be thought of as a property that is related to the characteristics of the fracture processes, the micro-/meso-/macro-structural features and the intrinsic toughening mechanisms characterising the material under investigation [15]. As far as un-reinforced concrete is concerned, comprehensive experimental/theoretical

Fig. 1. Applications of extrusion based concrete printing in architecture, construction, and infrastructure. Top left: 640 m², 9.5 m high building in Dubai (image courtesy of Apis Cor). Top right: 10 m tower base for a wind turbine (image courtesy of COBOD). Bottom left: the 12 m by 16 m Striatus bridge, Venice, Italy, 2021 - Project by Block Research Group (BRG) at ETH Zurich, Zaha Hadid Architects Computation and Design Group (ZHACODE), in collaboration with incremental3D (in3D) and made possible by Holcim. Bottom right: double curved façade panels prototyped at Loughborough University in 2011.
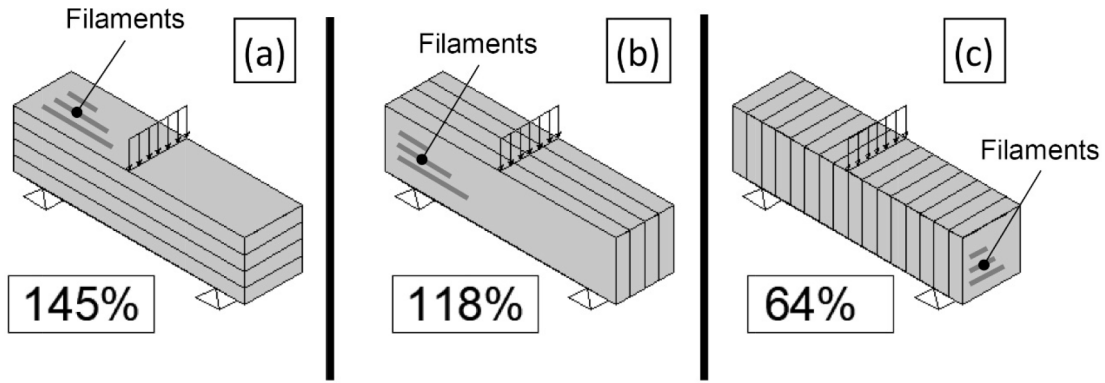
Fig. 2. Load direction and relative strength of 3DPC in relation to the filaments' interface (relative strength is a percentage of conventionally cast concrete) (a) perpendicular (b) longitudinal (c) lateral ().
Adapted from [8,13]

investigations [26–28] have demonstrated that the TCD critical distance is of the order of a few millimetres, with this holding true under either static, dynamic or high-cycle fatigue loading. This experimental evidence supports the idea that critical distance L is somehow linked with the features of the concrete morphology at a mesoscopic level - i.e. with the geometrical characteristics of the dominant source of inherent meso-structural heterogeneity.

In more general terms, it is well-known that, independently of their nature and characteristics, engineering materials always contain internal barriers. In terms of cracking behaviour/strength, these internal barriers can have a toughening effect since, under specific circumstances, they can affect/inhibit the crack propagation process. According to this physical model, it is logical to presume that the TCD critical distance should be of the same order of magnitude as the average spacing amongst adjacent barriers [23].

Based on the above considerations, the hypothesis can be formed that in un-reinforced cast concrete subjected to static/dynamic loading, cracks initiate predominantly in the highly stressed regions and propagate until their growth is either arrested or, at least, slowed down by the first aggregates that play the role of internal meso-structural barriers. Thus, it is logical to conclude that critical distance L in plain cast concrete approaches the average distance between the crack initiation locations and the first aggregates, with these aggregates acting as barriers that influence the crack growth process [29].

Having defined the necessary material length scale parameter, σ_{eff} can be calculated by adopting different definitions for the integration domain being used. In particular, according to the simplest formalisations of the TCD, the effective stress can be calculated in the form of either the Point Method (PM) or the Line Method (LM) as follows (see Fig. 3) [30]:

$$\sigma_{eff} = \sigma_y \left(x = \frac{L}{2} \right) - \text{Point} \quad \text{Method} \quad (\text{Fig.} \quad 3b) \tag{2}$$

$$\sigma_{eff} = \frac{1}{2L} \int_0^{2L} \sigma_y(x)dx - \text{Line} \quad \text{Method} (\text{Fig.} \quad 3c) \tag{3}$$

In other words, the PM assumes that the effective stress is equal to the stress acting at a distance from the assessed crack/notch tip equal to L/2 (Fig. 3b). In contrast, the LM effective stress is determined by averaging the local linear-elastic stress over a straight line having length equal to 2L (Fig. 3c).

It is worth pointing out here that there are also a bi-dimensional version (Area Method) and a three-dimensional formalisation (Volume Method) of the TCD [30]. The Area Method postulates that the effective stress is calculated by averaging the linear-elastic stress over a semi-circular area centred at the notch/crack tip and having radius equal to L. In a similar way, the Volume Method defines σ_{eff} by averaging the linear-elastic over a hemisphere centred again at the tip of the considered stress raiser, with the radius being taken equal to 1.54L [30].

Having calculated the design effective stress according to one of the strategies briefly reviewed above, the TCD assumes that a cracked/flawed/notched brittle material under static loading will fail as soon as σ_{eff} becomes equal to σ_{UTS} [15].

As far as cracks and flaws are concerned, one of the key feature of the TCD is that this theory is capable of describing and modelling the gradual transition from the short- to the long-crack/defect regime [31,32]. In more detail, if Westergaard's analytical solution [33] is used to describe the stress field in the vicinity of the tip of a crack loaded in tension, the PM and LM can be rewritten as follows [15]:

$$\sigma_f = \sigma_{UTS} \sqrt{1 - \left(\frac{a}{a + \frac{L}{2}} \right)^2} - \text{Point} \quad \text{Method} \tag{4}$$

$$\sigma_f = \sigma_{UTS} \sqrt{\frac{L}{a + L}} - \text{Line} \quad \text{Method} \tag{5}$$

(caption on next page)
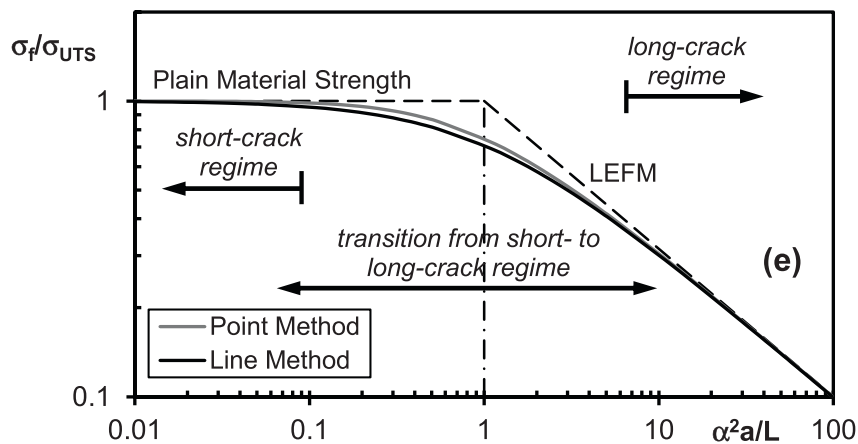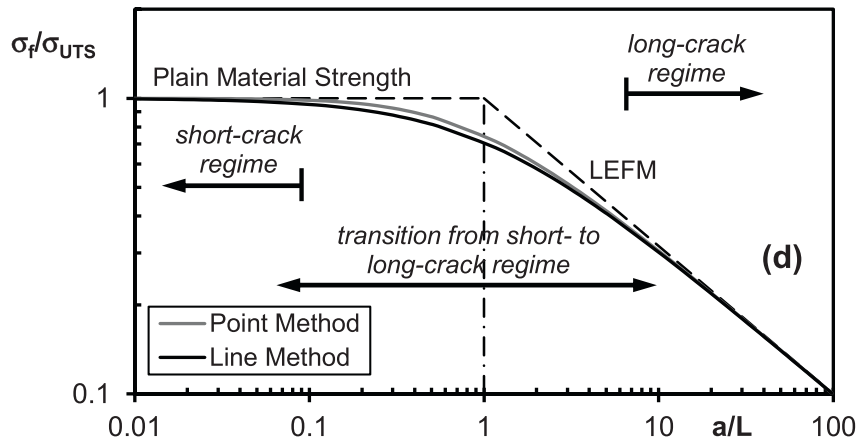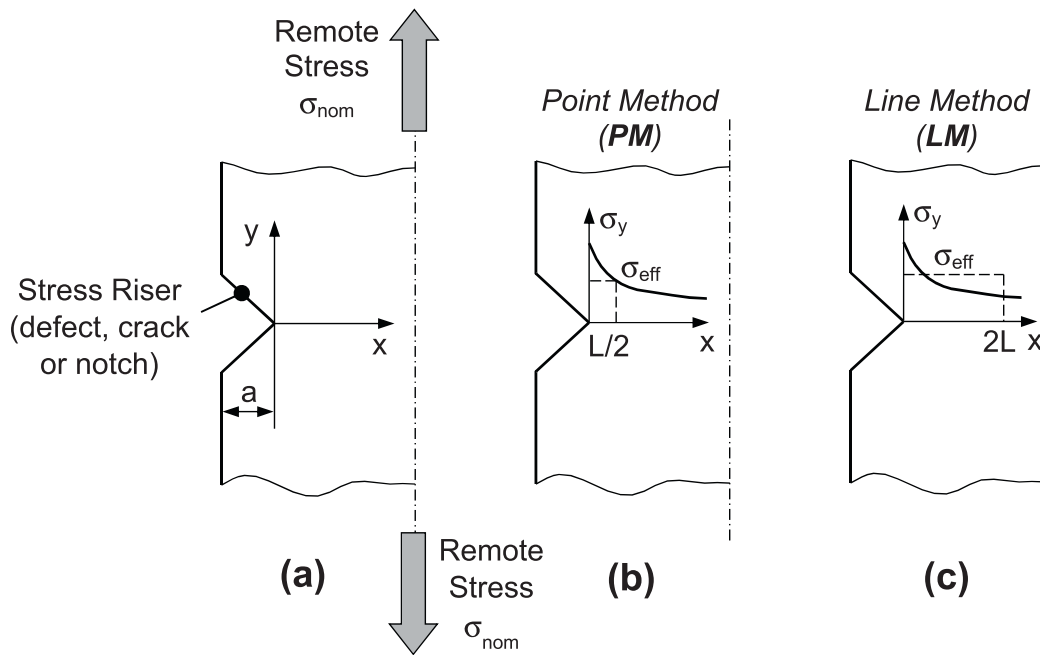
Fig. 3. Component containing either a defect, a crack, or a notch loaded in tension (a); the TCD applied in the form the PM (b) and the LM (c); normalised Kitagawa–Takahashi for the case of a central-crack in an infinite plate (d) and for the case of a stress riser with shape factor, α, different from unity (e).

In Eqs (4) and (5) σ_f is used to denote the nominal gross stress in the incipient failure condition, whereas a denotes the semi-length of the crack being analysed. σ_{UTS} is the ultimate tensile strength.

The normalised Kitagawa–Takahashi chart seen in Fig. 3d confirms that Eqs (5) and (6) are successful in linking the short-crack/defect zone with the long-crack/defect region. In more detail, Eqs (4) and (5) are seen to gradually approach the plain material strength, σ_{UTS}, as the size of the crack/defect decreases. In contrast, in the presence of large cracks/defects, the PM and LM formalised according to Eqs (4) and (5) fully agree with the estimates obtained via classic Linear Elastic Fracture Mechanics (LEFM) and based on the material fracture toughness. When the semi-length of the crack being analysed approaches L (i.e. when the a to L ratio approaches unity), the chart of Fig. 3d makes it evident that the use of the PM results in predictions that are slightly less conservative that those obtained through the LM.

Since Eqs (4) and (5) were derived based on the stress described through Westergaard's solution [33], strictly speaking, the chart seen in Fig. 3d is valid solely in the presence of a central crack in an infinite plate loaded in tension. However, the validity of this schematisation can be extended to other cases by taking full advantage of the LEFM shape factor, α, to calculate an equivalent crack length as follows [34–36]:

$$a_{eq} = \alpha^2 a \tag{6}$$

In the LEFM framework, the shape factor is a geometrical parameter that allows position and relative size of the crack as well as type of loading to be taken into account correctly when the Mode I stress intensity factor, K_I, is calculated through the following well-known definition [37]:

$$K_I = \alpha \bullet \sigma_{nom} \bullet \sqrt{\pi \bullet a} \Rightarrow \tag{7}$$

$$K_I = \sigma_{nom} \bullet \sqrt{\pi(\alpha^2 \bullet a)} = \sigma_{nom} \bullet \sqrt{\pi \bullet a_{eq}} \tag{8}$$

In Eqs (7) and (8) σ_{nom} is the nominal gross stress determined at the component section containing the crack/defect being assessed. Via equivalent crack length a_{eq} the static strength of cracked/flawed structural details having different values of the shape factor can all be brought back to the case of a central through-thickness crack in an infinite plate loaded in tension. By so doing, as per Fig. 3e, Eqs. (4) and (5) can be used as they are to model the transition from the short- to the long-crack/defect regime independently of position and size of the crack as well as independently of type of loading (i.e., either tension or bending) [34–36].

The body of theoretical knowledge briefly reviewed in the present section will be used in what follows to attempt to model the detrimental effect of cracks and manufacturing defects on the static strength of 3D-printed concrete.

3. Manufacturing of the 3D-printed concrete slabs

The main materials used for manufacturing the concrete slabs consist of 52.5N CEM I Portland Cement, fly ash, silica fume, sand, and water in the proportions [%] 100/29/14/214/36, respectively. Polycarboxylate ester-based superplasticiser and amino tris (methylene phosphonic acid) based retarder were used to control the rheology of the mixture to satisfy printing requirements. The printable mixture was developed for high-performance concrete for a nominal compressive strength of 100 MPa and nominal flexural strength of 12 MPa, the development and applications' details of the printable mixture can be found in Refs [8,38,39].

The 3D printed concrete employed in the present investigation was manufactured using an ABB IRR 6640 6-axis robot to control the deposition of the pumped concrete mixture. A CAD model of the printed slabs (560 × 200 × 54 mm) was sliced and fed into the ABB robot studio to create the print tool path. Print speeds of 200, 225, and 250 mm/s using a nozzle diameter of 10 mm and a layer height of 6 mm were used for the additive manufacture of the samples. The concrete pump flow rate during printing was 0.72 L/min. Typical printed slabs are shown in Fig. 4. After printing, the slabs were covered for 24 h and cured in water for 28 days. This was followed by wet slicing to desired sizes using a clipper saw with diamond blades.

The equivalent print speed for the constant 0.72 L/min flow rate is 200 mm/s; 225 and 250 mm/s were selected to intentionally create voids (manufacturing defects) in the specimen by causing volume mismatch. That is, the concrete pump flow rate does not match the 225 and 250 mm/s higher print speed. Higher printing speed causes thinning of the deposited filament and essentially creates voids between the filaments as shown in Fig. 4. 250 mm/s print speed accentuates these effects. These manufacturing defects represent one of the worst-case scenarios that weakens interlayer bond strength in extrusion-based additive manufacturing of concrete and intensifies the anisotropic mechanical properties. It should be noted that the other critical factor of moisture loss due to environmental conditions can be assumed to be negligible under laboratory conditions (air temperature 21 ± 0.5 °C and 65% relative humidity) and with an interlayer time lesser than 1 min.

4. 3D-printed concrete specimens and static testing

The concrete slabs additively manufactured as described in the previous section were saw-cut to make rectangular parallelepipeds having width, W, in the range 44–53 mm and thickness, B, in the range 34–56 mm (Fig. 5). The exact values of relevant dimensions W and B characterising the specimens being tested are summarised in Tables 1-4. The rectangular section beams used to make the

specimens were cut so that the printing direction was either parallel, $\theta_p = 0°$, or perpendicular, $\theta_p = 90°$, to the specimen longitudinal axis.

In order to better understand the effect of the additive manufacturing process on the mechanical behaviour/strength of the concrete mix being used, a number of specimens were made also from a slab fabricated through a conventional casting process.

All the specimens were tested under three-point bending up to complete breakage by using a Shimadzu axial machine. The results were generated under quasi-static loading, i.e. by setting the displacement equal to 33.3 N/sec [40]. As reported in Tables 1-4, the span, S, between the lower rollers (Fig. 5) was set equal to either 60 mm, 80 mm, or 100 mm. Independently of geometry/characteristics of the specimens, the failure bending stress was always calculated via the maximum value of the force recorded during testing.

The results generated from the plain specimens (Fig. 5a) are summarised in Table 1. For any specimen, other than the relevant dimensions of the cross-section and the length of the span, the table reports also the failure force, F_f, and the corresponding flexural strength, σ_{FS}. The values of the flexural strength listed in Table 1 make it evident that, in the absence of visible manufacturing defects, the strength of the 3D-printed concrete with $\theta_p = 0°$ was seen to be close to the strength characterising the conventional cast material.

Table 2 summarises the results that were generated by testing the specimens containing the crack-like sharp notches with depth a varying in the range 2–27 mm (Fig. 5b). These notches were fabricated using a circular tip blade having thickness equal to 2.6 mm. Fig. 6 shows some examples of the cracking behaviour displayed by these specimens. As expected, in all the samples the cracks were seen to initiate at the tips of the crack-like notches and then grow (predominately) along directions parallel to the notch bisectors (conventional Mode I-governed propagation). As to the results reported in Table 2, it is interesting to point out that, as observed in other 3D-printed concrete-related investigations [41] as well as in other fused filament fabricated materials [42,43], since the specimens were all manufactured flat on the built surface, the influence of angle θ_p on the material strength was seen to be (for the specific mix/printing technology being used) so little that it could be disregarded, with this resulting just in a little loss of accuracy.

Table 3 lists the results from the experiments that were run to investigate the detrimental effect of the surface roughness resulting from the deposition filaments (see Fig. 5c). For these specimens, the valleys characterising the surface texture were modelled as cracks. The depth, a, of these equivalent cracks was defined as the maximum valley depth below the filament peaks in the vicinity of the failure location (see Fig. 5c). This simple geometrical definition for the depth of the equivalent cracks resulted in values of length a varying from 1.2 mm up to 3.5 mm (see Table 3). Fig. 7 shows two examples of the cracking behaviour observed in these specimens. According to this figure, the cracks were seen to initiate, at the section experiencing the maximum bending moment, from the local valley characterising the surface profile and then propagate along vertical directions (Mode I-dominated growth).

The results generated by testing the specimens containing manufacturing defects (Fig. 5d) are summarised in Table 4. According to the pictures reported in Fig. 5d, these specimens were fabricated so that 3D-printing-related manufacturing flaws were introduced mainly on the side undergoing tensile stress during testing. For a given vertical cross section, the defects were assumed to be interlinked, resulting in an equivalent crack having length, a, defined as shown in Fig. 5d and 8a. Further, in the regions containing a high density of defects, this idealised coalescence process resulting in an equivalent crack having length equal to a was supposed to be characterised by negligible bridging/bonding effects between adjacent filaments.

Turning to the observed cracking behaviour, due to the large density of defects being intentionally introduced during additive manufacturing, in the majority of the specimens the cracks initiated away from the cross-sections experiencing the maximum nominal bending moment (Fig. 8a). The crack initiation process was then followed by an initial propagation occurring mainly along vertical directions, with the crack paths gradually deflecting towards the force application point (Fig. 8). According to Fig. 8a, the horizontal distance between the crack initiation location and the cross-sectional area of maximum bending stress was denoted as O_S. The measured values for O_S are reported in Table 4. These off-centre initiations were simply due to the fact that, in the vicinity of the
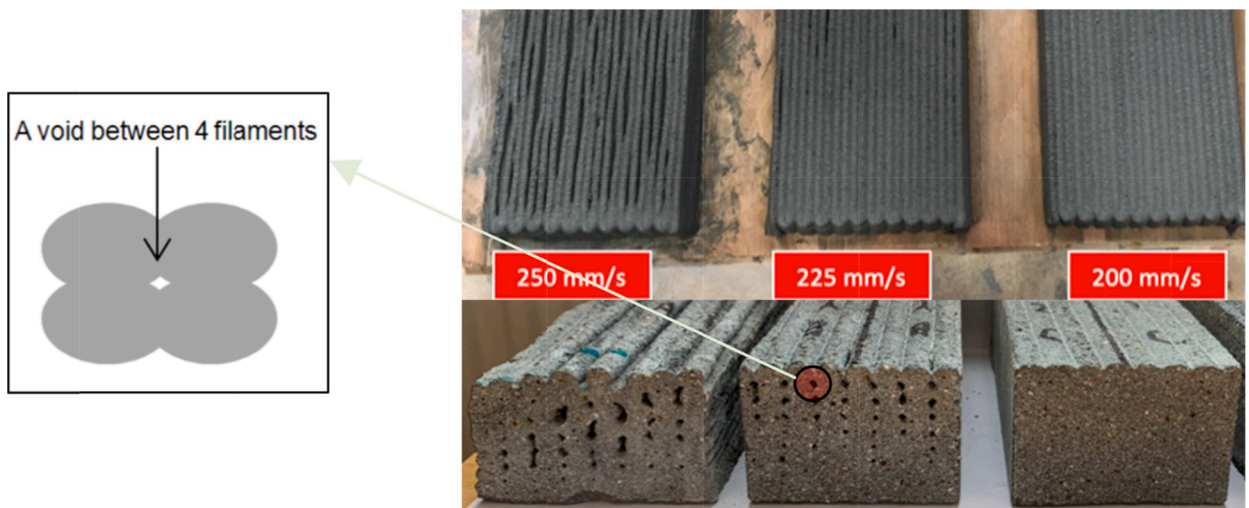

Fig. 4. Examples of 3D-printed concrete slabs specifically manufactured for the present study.

regions experiencing the maximum bending stress, cracks tended to start at those sections representing the weakest link in the specimen's structural chain.

The experimental results discussed above and summarised in Tables 1-4 will be used in the following section to check whether the TCD is successful in modelling the detrimental effect of cracks and manufacturing defects in 3D-printed concrete.

5. Theory of critical Distances and defects/cracks in 3D-printed concrete

In order to check the accuracy and reliability of the TCD in assessing the static strength of 3D-printed concrete containing cracks and defects, the first step was to determine the fracture toughness associated with the results listed in Tables 1-4. To this end, all the specimens being tested were modelled numerically using Finite Element (FE) code ANSYS®. The samples were all schematised as single edge notched bend (SE(B)) beams, with the notch tip radius being set invariably equal to zero. Any individual FE model was built using the relevant geometrical dimensions (i.e., B, W, S, a, and O_S) reported in Tables 2-4. The crack length, a, for the various cases being considered was defined as discussed in the previous section (see Fig. 5). The stress analysis was performed using bi-dimensional elements with thickness PLANE183, with the mesh being gradually refined in the vicinity of the crack tip in order to reach convergence in the determination of the stress intensity factor.

In terms of local stress distribution, it is well-known that in sharply notched beams subjected to bending the level of stress multiaxiality in the notch tip region varies across the thickness. In particular, the stress state is biaxial on the lateral surfaces, with the largest level of stress triaxility being reached at the beam mid-section [44]. Accordingly, cracks should initiate predominately in a region close to the mid-section of the beam, i.e., in a region where the extent of the damage associated with the stress triaxiliatiy level reaches its maximum value. Unfortunately, this idealised schematisation does not strictly apply to the specimens being tested. In fact, given the fabrication process as described in Section 3 and 4, the concrete being manufactured was seen to be highly non-uniform at a local/mesoscopic level. Further, as described in detail in Section 4, the real geometries of the specimens being tested differed massively from the idealised geometry of a beam containing a longitudinal slit. Having acknowledge these intrinsic limitations, the numerical stress analyses was then performed by solving simple bi-dimensional model, i.e. by implicitly assuming a uniform distribution of the stress across the thickness. This straightforward stress analyses approach is commonly used to solve standard LEFM problems, with this simplifying assumption resulting just in a little loss of accuracy [37]

Turning back to the numerical analyses being performed, by following the simple, standard procedure described above, the linear-elastic stress distribution along the crack bisector was determined in the incipient failure condition - i.e., by setting in the FE models the applied force equal to F_f. These stress fields were used to determine the stress intensity factors as well as the shape factors as explained in what follows.

According to the local system of coordinates seen in Fig. 3a, the stress intensity factor is defined in a rigorous way as [36]:
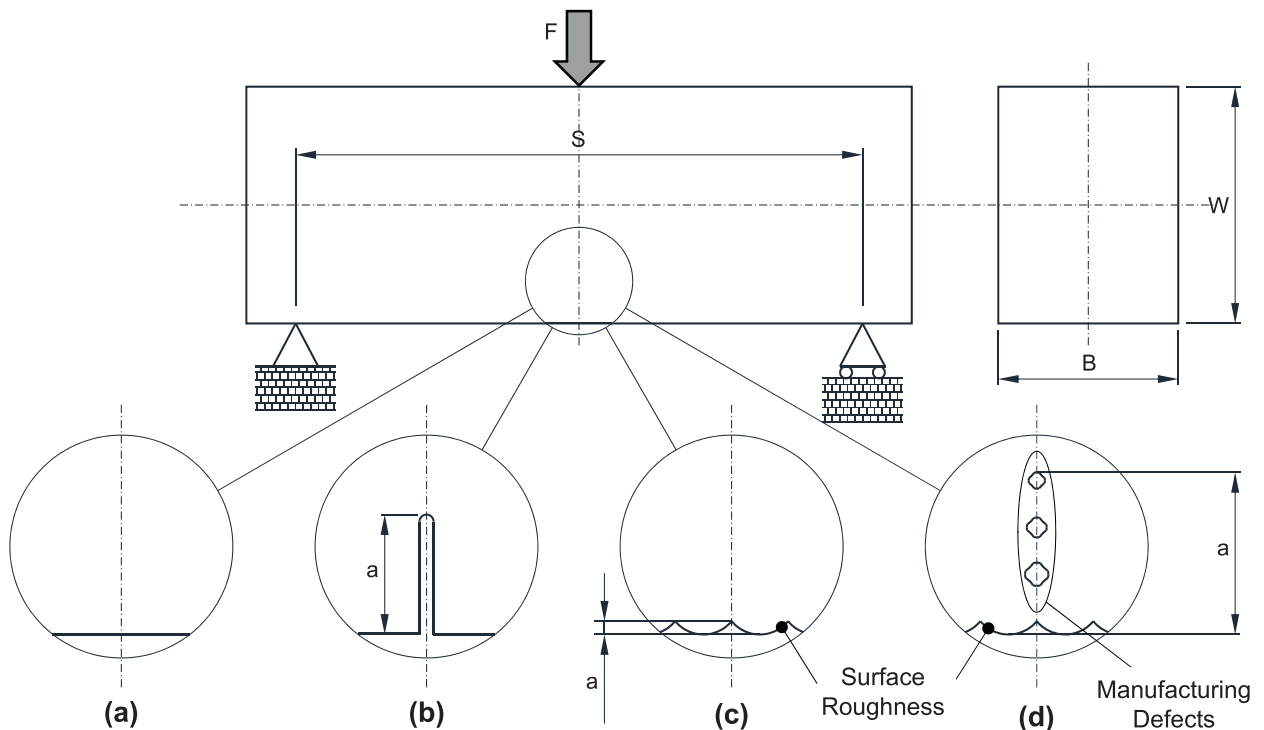
Fig. 5. 3D-printed specimens tested under three-point bending: plain specimen (a); specimen containing a saw-cut crack-like sharp notch (b); specimen (with $\theta_p = 90°$) weakened by surface roughness (c); specimen (with $\theta_p = 90°$) weakened by manufacturing defects (d).

Table 1

Summary of the experimental results generated by testing the plain specimens (Fig. 5a).

Code	W [mm]	B [mm]	S [mm]	θ_P [°]	F_f [kN]	σ_{FS} [MPa]
$C_{40,\,40}$[1]	41.0	39.9	100	–	5.6	12.5
$A1_{50,\,50}$	50.4	55.7	100	0	14.2	15.0
$A2_{50,\,50}$	52.6	50.8	100	0	12.4	13.2
$A3_{50,\,40}$	52.7	40.1	100	0	9.7	13.0
$A4_{50,\,40}$	51.3	39.9	100	0	9.5	13.5

[1] Cast concrete.

Table 2

Summary of the experimental results generated by testing the specimens containing saw-cut crack-like notches (Fig. 5b).

Code	W [mm]	B [mm]	a [mm]	S [mm]	θ_P [°]	F_f [kN]	K_C [MPa m$^{1/2}$]	α
C_1[1]	41.0	39.9	10.2	60	–	4.80	1.10	0.95
A1_1	50.4	55.7	12.2	60	0	11.30	1.45	1.03
A2_1	52.6	50.8	14.1	60	0	8.80	1.24	1.04
A3_1	52.7	40.1	13.9	60	0	7.30	1.29	1.04
A4_1	51.3	39.9	13.4	60	0	5.90	1.07	1.03
B1	53.3	37.5	14.6	60	90	4.80	0.91	1.05
C_2[1]	41.0	39.9	19.7	60	–	2.60	1.05	1.21
A1_2	50.4	55.7	25.1	60	0	4.80	1.07	1.25
A2_2	52.6	50.8	26.0	60	0	5.60	1.27	1.24
A3_2	52.7	40.1	25.5	60	0	4.30	1.19	1.21
A4_2	51.3	39.9	25.5	60	0	4.00	1.20	1.24
A5_2	53.3	37.5	26.9	60	90	4.50	1.39	1.26
$AC1_{0.05}$	44.8	31.4	1.9	60	90	7.59	0.94	1.12
$AC2_{0.05}$	45.5	32.2	1.8	60	90	9.15	1.04	1.11
$AC3_{0.05}$	44.2	31.8	2.5	60	90	5.68	0.80	1.10
$AC1_{0.11}$	44.7	32.0	4.6	60	90	7.51	1.32	1.04
$AC2_{0.11}$	44.6	32.1	4.7	60	90	8.41	1.48	1.03
$AC3_{0.11}$	44.1	31.8	5.1	60	90	4.83	0.90	1.01

[1] Cast concrete.

Table 3

Summary of the experimental results generated by testing the specimens weakened by surface roughness (Fig. 5c).

Code	W [mm]	B [mm]	a [mm]	S [mm]	θ_P [°]	F_f [kN]	K_C [MPa·m$^{1/2}$]	α
$B1_{50,\,40}$	53.3	37.5	1.2	100	90	7.92	0.75	1.09
$B2_{50,\,40}$	53.7	37.8	3.5	80	90	5.38	0.64	1.03
$B3_{50,\,40}$	53.3	41.2	3.1	80	90	6.62	0.70	1.04
$B4_{50,\,40}$	52.9	42.2	1.3	80	90	9.14	0.64	1.08

Table 4

Summary of the experimental results generated by testing the specimens containing manufacturing defects (Fig. 5d).

Code	W [mm]	B [mm]	a [mm]	S [mm]	θ_P [°]	O_S [mm]	F_f [kN]	K_C [MPa m$^{1/2}$]	α
B	50.4	39.3	29.0	100	90	10.5	3.19	1.95	1.70
B-S1	50.4	39.3	29.0	80	90	10.0	2.64	1.22	1.70
B-S2	50.4	39.3	29.0	80	90	10.0	3.48	1.61	1.70
BD4	51.3	39.2	36.0	80	90	18.8	1.99	1.09	2.65
BD5	51.2	37.9	36.0	80	90	18.5	2.01	1.17	2.67
BD6	50.8	38.4	37.0	80	90	19.0	1.74	1.13	3.00
BD7	52.9	41.0	23.0	80	90	10.0	3.90	1.03	1.25
BD8	52.1	41.1	25.0	80	90	9.3	2.96	0.93	1.36
BD9	50.8	37.2	33.0	80	90	0.0	1.92	1.67	2.16
BD10	49.4	34.6	37.0	80	90	0.0	0.75	1.21	3.33

Code	a/W	Side View	Crack Surfaces
AC2$_{0.05}$	0.04		
AC2$_{0.11}$	0.10		
A2_1	0.27		
A2_2	0.49		

Fig. 6. Examples of the cracking behaviour displayed by the specimens containing saw-cut crack-like sharp notches of different depth (Fig. 5b).

$$K_I = \sqrt{2\pi} \bullet \lim_{x \to 0} \left[\sigma_y(x) \bullet \sqrt{x} \right] \tag{9}$$

Based on definition (9), K_I in the vicinity of the crack tip can be calculated through the FE method as follows:

$$K_{I,FEM} = \sigma_{y,FEM}(x)\sqrt{2\pi \bullet x} \tag{10}$$

where $\sigma_{y,FEM}(x)$ is used to denote the distribution (along axis x) of normal stress σ_y determined numerically. Ultimately, by combining the engineering definition for K_I given by Eq. (7) together with Eq. (10), the LEFM shape factor is estimated as:
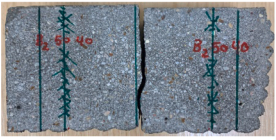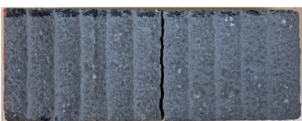
Code	a/W	Side View	Bottom View	Crack Surfaces
B2$_{50, 40}$	0.07			
B3$_{50, 40}$	0.06			

Fig. 7. Examples of the cracking behaviour displayed by the specimen (with $\theta_p = 90°$) weakened by surface roughness (Fig. 5c).
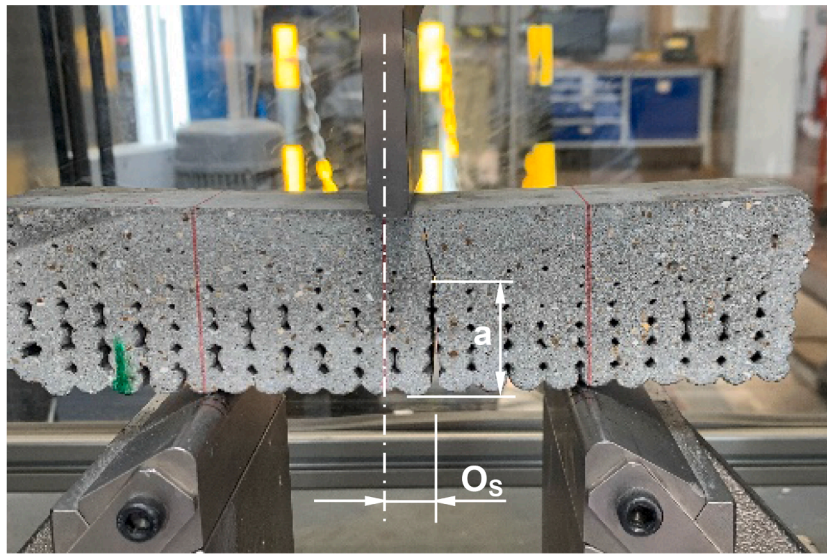
(a)

Code	a/W	Side View	Crack Surfaces
B-S2	0.58		
BD5	0.70		
BD8	0.48		
BD9	0.65		

(b)

Fig. 8. Examples of the cracking behaviour displayed by the specimens (with $\theta_p = 90°$) weakened by manufacturing defects (Fig. 5d).

$$\alpha = \frac{K_{I,FEM}}{\sigma_{nom}\sqrt{\pi \bullet a}} = \frac{\sigma_{y,FEM}(x)\sqrt{2\pi \bullet x}}{\sigma_{nom}\sqrt{\pi \bullet a}} \qquad (11)$$

This simple strategy was used to determine the necessary shape factors, so that the equivalent crack length, a_{eq}, could be calculated for any specimen being tested according to definition (6). Fig. 9 shows an example visualising the procedure that was followed to determine numerically the fracture toughness, K_C – i.e., the stress intensity factor in the incipient failure condition.

The values of the fracture toughness, K_C, and the shape factor, α, determined according to the numerical procedure described above are listed in Tables 2-4 for all the experimental results being generated.

Having determined the LEFM shape factors for the cracked/flawed concrete specimens being tested, the subsequent step was to determine the material properties that were needed to apply the TCD.

The plain material flexural strength was estimated by simply averaging the values obtained experimentally by testing the un-notched 3D-printed concrete specimens. By so doing, as per the values listed in Table 1, the plain material flexural strength, σ_{FS}, was then taken equal to 13.7 MPa.

Turning to the toughness characterising the additively manufactured concrete under investigation, initially, it is important to observe that, according to Table 2, the K_C values for the cast material were seen to be very close to the corresponding values determined from the additively manufactured specimens. This holds true for geometrical ratio a/W equal both to ≈0.25 and to ≈0.5. Accordingly, the two results generated by testing cast specimens containing crack-like notches were used according to the TCD-based strategy proposed and validated in Ref. [45] to estimate K_{IC}. This simple procedure returned a value for the plane strain fracture toughness, K_{IC}, equal to 1.2 MPa·m$^{1/2}$. This approach allowed us to determine the intrinsic material fracture toughness, i.e. a K_{IC} value determined by disregarding any possible effects associated with the additive manufacturing process.

As to the determination of the fracture toughness, it is important to point out also that, due to some geometrical constrains characterising the testing facilities available in the Sheffield Structures Laboratory, it was not possible for us to determine K_{IC} as recommended by RILEM [46]. However, since the ultimate goal of the present investigation was to check the accuracy of the TCD in modelling the detrimental effect of cracks/defects in 3D-printed concrete, it was considered to be reasonable to use an experimental strategy based on the TCD itself to derive the necessary material properties.

Having determined σ_{FS} and K_{IC} for the 3D-printed concrete under investigation, definition (1) was used to estimate the critical distance value – with σ_{UTS} being obviously replaced with σ_{FS} [15]. This simple calculation resulted in a material critical length, L, equal to 2.4 mm.

The reference material properties determined according to the reasoning summarised above together with the experimental results listed in Tables 2-4 were then used to build the Kitagawa–Takahashi diagrams seen in Fig. 10. These charts summarise the overall accuracy of the TCD - used in the form of the PM, Eq. (4), and LM, Eq. (5) - in estimating the static strength of 3D-printed concrete in the presence of localised stress concentration phenomena.

In order to quantify the accuracy of the TCD in estimating the experimental results summarised in Tables 2-4, the charts of Fig. 10 show not only the level of accuracy reached by applying the PM, Eq. (4), and LM, Eq. (5), but also the associated error bands. These bands were determined by calculating the error as follows:

$$Error = \frac{\sigma_f - \sigma_{f,exp}}{\sigma_{f,exp}} \bullet 100 \, [\%] \qquad (12)$$

where σ_f is the nominal gross stress in the incipient failure condition estimated according to either Eq. (4) or Eq. (5), whereas $\sigma_{f,exp}$ is the corresponding experimental value. As per definition (12), the error calculation shows if the proposed method predicts breakage conservatively or non-conservatively by assigning either positive or negative sign, respectively.

The diagrams of Fig. 10 make it evident that the use of the TCD resulted in a remarkable level of accuracy, with this holding true
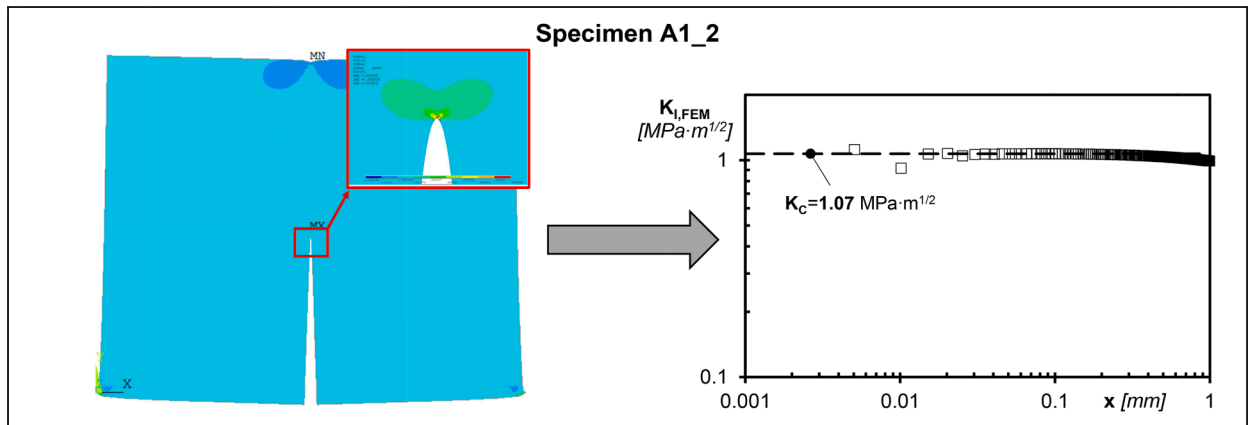

Fig. 9. Example showing the FE-based procedure followed to determine, in the incipient failure condition, the values of the fracture toughness, K_C.

independently of the type of local stress raiser being analysed. In particular, the use of the TCD to assess the strength of 3D-printed concrete is seen to result in estimates falling in an error interval of ± 30%. This result is certainly satisfactory especially in light of the fact that the TCD is capable of returning the same level of accuracy (i.e., ±30%) also when it is employed to predict the strength of notched un-reinforced cast concrete under Mode I [27,28] and Mixed Mode I/II loading [28].

Turning back to the charts of Fig. 10, both the PM and LM were seen to be capable of correctly modelling the presence of saw-cut crack-like notches, with this holding true independently of the 3D-printing direction.

As far as the effect of the surface finishing is concerned, the charts of Fig. 10 demonstrate that the surface roughness associated with the 3D-printed concrete filaments did reduce the overall strength of the material, with the reduction in strength being in the range 15%-25%. While this is an aspect that must certainly be taken into account in situations of practical interest, the relevant result is that the TCD is clearly capable of accurately capturing and modelling this phenomenon.
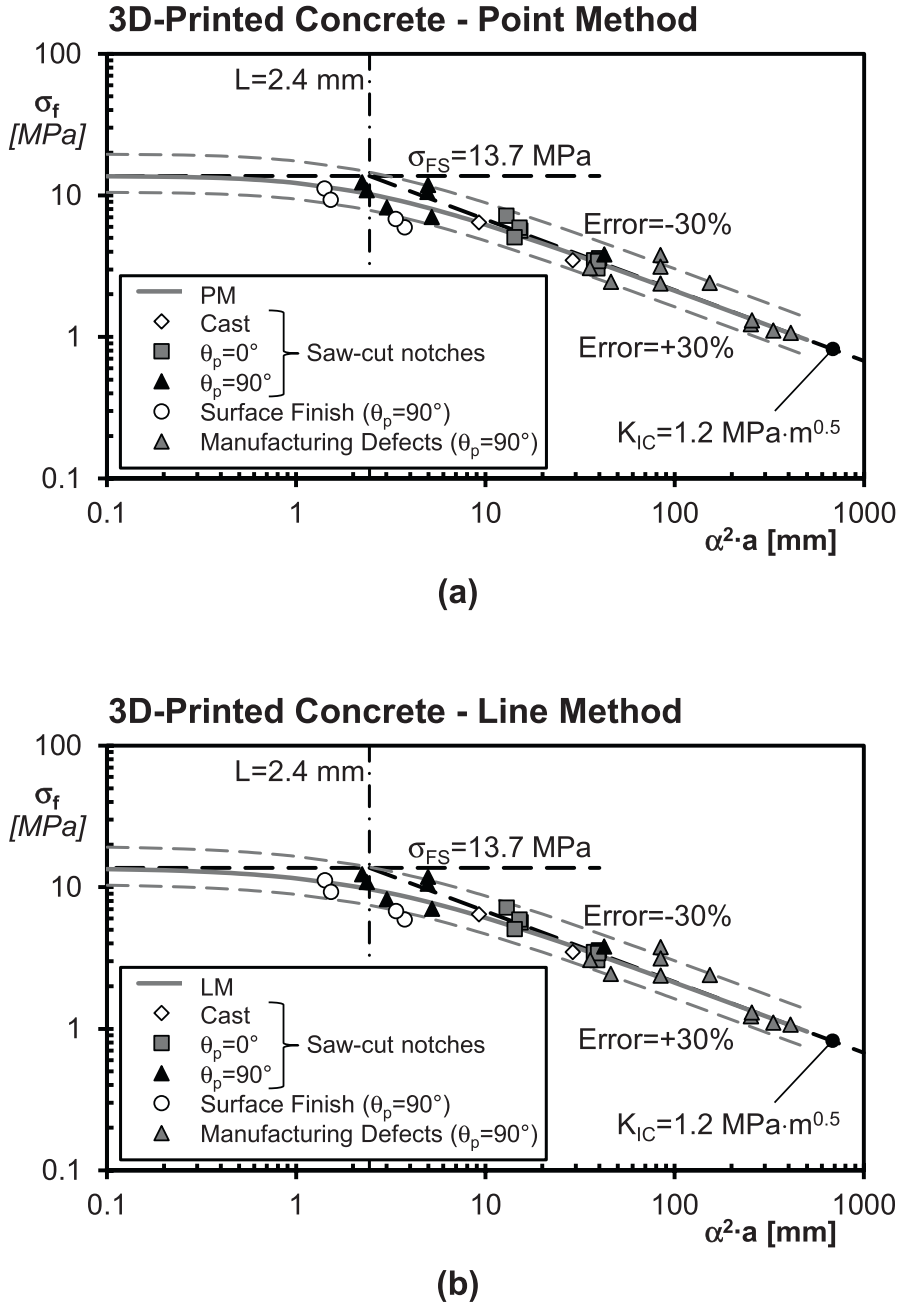

Fig. 10. Accuracy of the TCD in modelling the detrimental effect of cracks and defects in 3D-printed concrete loaded in three-point bending.

Finally, the charts of Fig. 10 make it clear that the equivalent crack length as defined in Fig. 5d allowed the TCD to predict in a very accurate way also the detrimental effect of manufacturing defects introduced during the 3D-printing process. It is important to point out here that the nominal failure stress, σ_f, used to report these experimental results in the charts of Fig. 10 was always calculated at the experimentally observed fracture section (see Fig. 8a).

As to the accuracy of the TCD in modelling the static strength of 3D-printed concrete, it is important to point out that the graphs of Fig. 10 were built by considering experimental results all generated by testing specimens having similar relevant dimensions (see Tables 1-4). While by its nature the TCD is seen to be capable of modelling the scale effect [15], the results being generated and discussed in the present study does not allow any relevant conclusions about TCD, scale effect and 3D-printed concrete to be drawn. Accordingly, more experimental work should be undertaken to investigate the accuracy of the TCD in modelling the fracture and size effect in 3D-printed concrete.

Based on the sound agreement between experimental results and predictions shown in Fig. 10, it is possible to conclude by observing that, clearly, the TCD can be seen not only as a powerful static assessment method, but also as a reliable tool capable of guiding and informing the manufacturing process so that components having the wanted mechanical properties and strength can be fabricated effectively.

6. Conclusions

The ultimate goal of the present research work was to formulate and validate a novel TCD-based methodology suitable for assessing the detrimental effect of manufacturing flaws, cracks and defects in additively manufactured concrete. The accuracy and reliability of this technique was tested against a large number of experimental results from 3D-printed concrete specimens weakened by saw-cut crack-like notches, surface roughness and manufacturing defects.

Based on the generated experimental results as well as on the performed theoretical and numerical analyses, it is possible to draw to the conclusions listed below.

- For the specific concrete mix/manufacturing technology used in the present investigation, the strength and toughness of the cast material are seen to be similar to those characterising the 3D-printed concrete.
- The surface roughness due to the 3D-printed filaments of concrete is seen to reduce the static strength, with the observed reduction being in the range 15%-25%.
- The presence of internal manufacturing flaws is seen to lower markedly the strength of the 3D-printed concrete.
- The TCD is successful in modelling the static strength of 3D-printed concrete as the surface roughness due to the manufacturing process changes.
- The TCD is capable of accurately model the detrimental effect of cracks and manufacturing defects, with this holding true independently of size and geometrical features of the stress raiser being assessed.
- The proposed TCD-based technique can be applied by post-processing simple linear-elastic FE models done using commercial codes.
- More work needs to be done in this area to extend the use of this theoretical framework to reinforced 3D-printed concrete.

CRediT authorship contribution statement

N. Alanazi: Writing – review & editing, Investigation, Validation, Data curation, Formal analysis. **J.T. Kolawole:** Writing – review & editing, Validation, Investigation. **R. Buswell:** Writing – review & editing, Supervision, Project administration, Funding acquisition. **L. Susmel:** Writing – original draft, Investigation, Validation, Formal analysis, Methodology, Supervision, Project administration, Funding acquisition.

Declaration of Competing Interest

The authors declare that they have no known competing financial interests or personal relationships that could have appeared to influence the work reported in this paper.

Acknowledgments

References

[1] Buswell RA, Leal de Silva WR, Jones SZ, Dirrenberger J. 3D printing using concrete extrusion: A roadmap for research. Cem Concr Res 2018;112:37–49.
[2] Ma G, Buswell R, Leal da Silva WR, Wang L, Xu J, Jones SZ. Technology readiness: A global snapshot of 3D concrete printing and the frontiers for development. Cem Concr Res 2022;156:106774.
[3] Lezama-Nicolás R, Rodríguez-Salvador M, Río-Belver R, Bildosola I. A bibliometric method for assessing technological maturity: the case of additive manufacturing. Scientometrics 2018;117:1425–52.

[4] Buswell RA, Leal da Silva WR, Bos FP, Schipper R, Lowke D, Hack N, et al. A process classification framework for defining and describing Digital Fabrication with Concrete. Cem Concr Res 2020;134:126426.
[5] Buswell R, Xu J, De Becker D, Dobrzanski J, Provis J, Kolawole JT, et al. Geometric quality assurance for 3D concrete printing and hybrid construction manufacturing using a standardised test part for benchmarking capability. Cem Concr Res 2022;156:106773.
[6] Wolfs RJM, Salet TAM, Roussel N. Filament geometry control in extrusion-based additive manufacturing of concrete: The good, the bad and the ugly. Cem Concr Res 2021;150:106615. https://doi.org/10.1016/j.cemconres.2021.106615.
[7] Baduge SK, Navaratnam S, Abu-Zidan Y, McCormack T, Nguyen K, Mendis P, et al. Improving performance of additive manufactured (3D printed) concrete: A review on material mix design, processing, interlayer bonding, and reinforcing methods. Structures 2021;29:1597–609.
[8] Le TT, Austin SA, Lim S, Buswell RA, Law R, Gibb AGF, et al. Hardened properties of high-performance printing concrete. Cem Concr Res 2012;42:558–66.
[9] Wolfs RJM, Bos FP, Salet TAM. Hardened properties of 3D printed concrete: The influence of process parameters on interlayer adhesion. Cem Concr Res 2019; 119:132–40.
[10] Sanjayan JG, Nematollahi B, Xia M, Marchment T. Effect of surface moisture on inter-layer strength of 3D printed concrete. Constr Build Mater 2018;172: 468–75.
[11] Panda B, Paul SC, Mohamed NAN, Tay YWD, Tan MJ. Measurement of tensile bond strength of 3D printed geopolymer mortar. Measurement 2018;113:108–16.
[12] Chen Y, Çopuroğlu O, Romero Rodriguez C, de Mendonca Filho FF, Schlangen E. Characterization of air-void systems in 3D printed cementitious materials using optical image scanning and X-ray computed tomography. Mater Charact 2021;173:110948.
[13] du Plessis A, Yadroitsev I, Yadroitsava I, Le Roux SG. X-Ray Microcomputed Tomography in Additive Manufacturing: A Review of the Current Technology and Applications.
[14] Babafemi AJ, Kolawole JT, Miah MJ, Paul SC, Panda B. A Concise Review on Interlayer Bond Strength in 3D Concrete Printing. Sustainability 2021;13:7137.
[15] Taylor D. The Theory of Critical Distances: A new perspective in fracture mechanics. Oxford, UK: Elsevier; 2007.
[16] Whitney JM, Nuismer RJ. Stress Fracture Criteria for Laminated Composites Containing Stress Concentrations. J Compos Mater 1974;8:253–65.
[17] Susmel L, Taylor D. The theory of critical distances to predict static strength of notched brittle components subjected to mixed-mode loading. Eng. Frac. Mech. 2008;75:534–50.
[18] Susmel L, Taylor D. On the use of the Theory of Critical Distances to predict static failures in ductile metallic materials containing different geometrical features. Engng Fract Mech 2008;75:4410–21.
[19] Yin T, Tyas A, Plekhov O, Terekhina A, Susmel L. A novel reformulation of the Theory of Critical Distances to design notched metals against dynamic loading. Mater Des 2015;69:197–212.
[20] Taylor D. Geometrical effects in fatigue: a unifying theoretical model. Int J Fatigue 1999;21(5):413–20.
[21] Susmel L, Taylor D. A novel formulation of the Theory of Critical Distances to estimate Lifetime of Notched Components in the Medium-Cycle Fatigue Regime. Fatigue Fract Engng Mater Struct 2007;30:567–81.
[22] Askes H, Livieri P, Susmel L, Taylor D, Tovo R. Intrinsic material length, Theory of Critical Distances and Gradient Mechanics: analogies and differences in processing linear-elastic crack tip stress fields. Fatigue Fract Engng Mater Struct 2013;36:39–55.
[23] Taylor D. The Theory of Critical Distances: A link to micromechanisms. Theor Appl Fract Mech 2017;90:228–33.
[24] Susmel L, Taylor D. The Theory of Critical Distances to estimate the static strength of notched samples of Al6082 loaded in combined tension and torsion. Part II: Multiaxial static assessment. Engng Fract Mech 2010;77(3):470–8.
[25] Ameri AAH, Davison JB, Susmel L. On the use of linear-elastic local stresses to design load-carrying fillet-welded steel joints against static loading. Engng Fract Mech 2015;136:38–57.
[26] Jadallah O, Bagni C, Askes H, Susmel L. Microstructural length scale parameters to model the high-cycle fatigue behaviour of notched plain concrete. Int J Fatigue 2016;82:708–20.
[27] Pelekis I, Susmel L. The Theory of Critical Distances to assess failure strength of notched plain concrete under static and dynamic loading. Engng Fail Anal 2017; 82:378–89.
[28] Alanazi N, Susmel L. Estimating Static/Dynamic Strength of Notched Unreinforced Concrete under Mixed-Mode I/II Loading. Eng Frac Mech 2020;240:107329.
[29] Alanazi N, Susmel L. Theory of Critical Distances and static/dynamic fracture behaviour of un-reinforced concrete: length scale parameters vs. material meso-structural features. Eng Frac Mech 2022;261:108220.
[30] Bellett D, Taylor D, Marco S, Mazzeo E, Guillois J, Pircher T. The fatigue behaviour of three-dimensional stress concentrations. Int J Fatigue 2005;27:207–21.
[31] Taylor D. Predicting the fracture strength of ceramic materials using the theory of critical distances. Engng Fract Mech 2004;71:2407–16.
[32] Susmel L, Askes H, Bennett T, Taylor D. Theory of Critical Distances vs. Gradient Mechanics in modelling the transition from the short- to long-crack regime at the fatigue limit. Fatigue Fract Engng Mater Struct 2013;36:861–9.
[33] Westergaard HM. Bearing pressures and cracks. J Appl Mech A 1939;61:49–53.
[34] Usami S. Short crack fatigue properties and component life estimation. In: Tanaka T, Jono M, Komai K, editors. Current Research on Fatigue Cracks, Current Japanese Materials Research Series, Vol. 1. The Society of Materials Science, Kyoto, Japan; 1985, pp. 119–147.
[35] Tanaka K. Short crack fracture mechanics in fatigue conditions. In: Tanaka T, Jono M, Komai K, editors, Current Research on Fatigue Cracks, Current Japanese Materials Research Series, Vo. 1. The Society of Materials Science, Kyoto, Japan; 1985, pp. 93–117.
[36] Atzori B, Lazzarin P, Meneghetti G. Fracture mechanics and notch sensitivity. Fatigue Fract Engng Mater Struct 2003;26(3):257–67.
[37] Anderson T. Fracture mechanics: fundamentals and applications. 3rd ed. USA: CRC Press; 2005.
[38] Le TT, Austin SA, Lim S, Buswell RA, Gibb AGF, Thorpe T. Mix design and fresh properties for high-performance printing concrete. Mater Struct 2012;45: 1221–32.
[39] Kinnell P, Dobranski J, Xu J, Wang W, Kolawole J, Hodgson J, et al., Precision manufacture of concrete parts using Integrated Robotic 3D Printing and Milling. In: Euspen's 21st International Conference & Exhibition, EUSPEN, Copenhagen, 2021 (www.euspen.eu).
[40] Anon., Testing hardened concrete - Flexural strength of test specimens. BS EN 12390-5:2019; 2019.
[41] Rehman AU, Kim J-H. 3D Concrete Printing: A Systematic Review of Rheology, Mix Designs, Mechanical, Microstructural, and Durability Characteristics. Materials 2021;14:3800.
[42] Ahmed AA, Susmel L. A material length scale based methodology to assess static strength of notched additively manufactured polylactide (PLA). Fatigue Fract Engng Mater Struct 2018;41:2071–98.
[43] Ng CT, Susmel L. Notch Static Strength of Additively Manufactured Acrylonitrile Butadiene Styrene (ABS). Addit Manuf 2020;34:101212.
[44] Meneghetti G, Susmel L, Tovo R. High-cycle fatigue crack paths in specimens having different stress concentration features. Engng Fail Anal 2007;14:656–72.
[45] Susmel L, Taylor D. The Theory of Critical Distances as an alternative experimental strategy for the determination of K_{Ic} and ΔK_{th}. Eng Fract Mech 2010;77: 1492–501.
[46] Shah SP. Determination of fracture parameters (Ksic and CTODc) of plain concrete using three-point bend tests. Mater Struct 1990; 23: 457-460 (RILEM TC 89-FMT).